

pubs.acs.org/JPCL Letter

# Voxelized Atomic Structure Potentials: Predicting Atomic Forces with the Accuracy of Quantum Mechanics Using Convolutional Neural Networks

Matthew C. Barry,\* Kristopher E. Wise, Surya R. Kalidindi, and Satish Kumar\*



Cite This: J. Phys. Chem. Lett. 2020, 11, 9093–9099



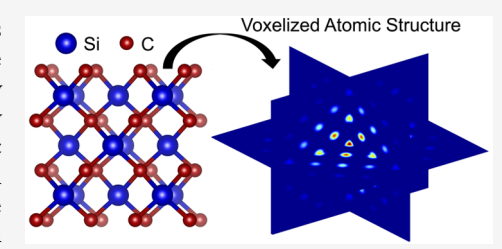
**ACCESS** 

III Metrics & More



Supporting Information

ABSTRACT: This paper introduces voxelized atomic structure (VASt) potentials as a machine learning (ML) framework for developing interatomic potentials. The VASt framework utilizes a voxelized representation of the atomic structure directly as the input to a convolutional neural network (CNN). This allows for high-fidelity representations of highly complex and diverse spatial arrangements of the atomic environments of interest. The CNN implicitly establishes the low-dimensional features needed to correlate each atomic neighborhood to its net atomic force. The selection of the salient features of the atomic structure (i.e., feature engineering) in the VASt framework is implicit, comprehensive, automated, scalable, and highly



efficient. The calibrated convolutional layers learn the complex spatial relationships and multibody interactions that govern the physics of atomic systems with remarkable fidelity. We show that VASt potentials predict highly accurate forces on two phases of silicon carbide and the thermal conductivity of silicon over a range of isotropic strain.

Atomic simulations are fundamental to understanding the physics of material and chemical systems. First-principles methods such as density functional theory  $(DFT)^{1,2}$  are highly accurate but impractical for physics involving more than a few hundred atoms and time scales  $\gtrsim 100$  ps. Empirical interatomic potentials<sup>3-12</sup> are much faster than first-principles methods and can scale to much larger atomic systems, but they are less accurate, difficult to develop, and lack transferability. Machine learning (ML) approaches offer new opportunities for the development of low-computational cost surrogate models trained to the expensive DFT computations. Notable successes have been reported in compound discovery (i.e., identification of specific compound chemistries that optimize a certain combination of desired properties)<sup>13-21</sup> and in the formulation of ML-based potentials.  $^{22-45}$ 

The value of an ML potential lies in how efficiently and accurately it learns the complex physics underlying the atomic interactions. The scope and efficacy of this learning is largely controlled by the input features selected for representing the atomic structure in the ML model (commonly referred to as feature engineering). For the development of ML-based potentials, feature engineering approaches have generally involved the identification of a small set of salient features guided by the known physics of atomic interactions. These approaches have led to the formulation and exploration of suitably defined kernel expansions<sup>22–24</sup> and/or projections.<sup>25–28</sup> Although these approaches have shown promise, the selection of such functions is largely ad hoc, and the resulting feature space is often an incomplete, oversimplified, and not easily interpretable representation of the atomic

structure. Furthermore, it is often impossible to systematically determine which combination of features offers the most important value for building high-fidelity ML models. In an effort to overcome these limitations, several approaches have been developed in which the feature engineering is performed implicitly through the training of neural networks (NNs) directly to the atomic positions and chemical elements involved.<sup>29–35</sup> For example, in message passing neural networks (MPNNs)<sup>31–35</sup> each atom is initially embedded with a feature vector based on its chemical species. The feature vectors are then passed through a series of atom and interaction layers, which operate on individual atoms and pairs of atoms, respectively. These layers are convolutional in the sense that the same operation is applied to each atom or pair of atoms in a layer and the interaction layers capture translationally invariant features based on the interatomic distances between pairs of atoms. However, these approaches still do not capture directly the true atomic structure, which is a three-dimensional (3D) space, as the input to the NN. Instead, the atomic structure is indirectly input into the NN using a list of relative atom center positions and element types.

In this article, we present an ML framework for developing interatomic potentials that utilizes directly the true atomic

Received: July 24, 2020 Accepted: September 27, 2020 Published: September 27, 2020





structure. In this framework, the physical volume around the atom of interest is mapped to a voxelized 3D domain. This voxelized atomic structure (VASt) representation is equivalent to capturing the atomic neighborhood as a digital 3D image, which is ideal as an input to convolutional neural networks (CNNs) for implicit feature engineering. CNNs have had great success in image analysis due to their ability to capture translationally invariant spatial features and naturally account for multiple local states per voxel (i.e., grayscale or red, green, blue (RGB)) via input channels. 46–50 In the context of VASt potentials, the calibrated convolutional layers of the CNN serve as a complex, nonlinear mapping from the voxelized representation of the atomic neighborhood to a low-dimensional feature space that is finally used to predict the target (i.e., output) net atomic force. Additionally, the CNN input channels naturally allow for the representation of multielement systems. Because the feature engineering (selection of the salient low-dimensional features) is comprehensive, automated, scalable, and highly efficient in CNNs, VASt potentials are able to learn implicitly the complex spatial relationships and multibody interactions that govern the physics of atomic

The VASt framework is tested with two case studies. First, we develop a VASt potential capable of predicting highly accurate interatomic forces on atomic environments of two phases of silicon carbide (SiC), namely, 3C-SiC and 6H-SiC, generated from ab initio molecular dynamics (AIMD)<sup>5</sup> simulations at 300 K. This study demonstrates that VASt potentials can successfully capture the diverse space of atomic environments spanned by multicomponent, multiphase systems and therefore are viable for general molecular dynamics (MD) applications. Second, we develop a VASt potential capable of accurately reproducing the thermal conductivity of crystalline silicon subjected to isotropic strain ranging from -0.035 to 0.035. Isotropic strain effects on the thermal conductivity of silicon have previously been studied using DFT with the Boltzmann transport equation (BTE)<sup>52</sup> and using equilibrium MD.<sup>53</sup> However, both methods face practical challenges. With the BTE, calculating the thermal conductivity for a single value of strain can require hundreds of DFT calculations on large supercells. 54,55 Repeating this process for each value of strain can be computationally infeasible. With MD, the accuracy of thermal conductivity calculations is dependent on the choice of empirical potential. In unstrained silicon, for example, the thermal conductivities at 300 K computed using the Stillinger-Weber<sup>11</sup> and Tersoff<sup>12</sup> potentials are  $\sim$ 700 and  $\sim$ 350 W/m K, <sup>56</sup> respectively, which both deviate substantially from the experimental value of ~150 W/m K.<sup>57</sup> Further, empirical potentials may fail in extreme conditions such as high strain. The Tersoff potential, for example, predicts that the thermal conductivity of silicon monotonically decreases from compression to tension,<sup>53</sup> whereas the BTE predicts that it remains relatively constant under compression and then decreases from equilibrium to tension.<sup>52</sup>

We use our VASt potential to compute thermal conductivity with the BTE in a highly accurate and computationally efficient manner by predicting the interatomic forces required for computing the second-order harmonic and third-order anharmonic interatomic force constants (IFCs). Previous ML approaches have proven to be capable of accurately reproducing second-order IFCs and phonon dispersion curves. 25,38-40,43-45 Very few studies, however, have successfully reproduced thermal conductivity, 39,40 which requires

third-order anharmonic IFCs that can be very sensitive to noise and therefore require very accurate forces. Korotaev et al.<sup>39</sup> computed the thermal conductivity of unstrained CoSb<sub>3</sub> skutterudite with both the BTE and MD using a moment tensor potential.<sup>27</sup> Babaei et al.<sup>40</sup> computed the thermal conductivity of unstrained silicon with the BTE using a Gaussian approximation potential.<sup>25</sup> Both studies demonstrate that these approaches can accurately predict the interatomic forces resulting from the small perturbations of atomic structure used to compute IFCs. However, by computing the thermal conductivity over a range of isotropic strain, we demonstrate that VASt potentials are not only sensitive to small perturbations of atomic structure, but are also consistent and can maintain this sensitivity over a large range of isotropic strain.

The positions of atom centers in the neighborhood of an atom of interest can be represented by a summation of delta functions as

$$\varphi(\mathbf{r}, Z) = \sum_{\mathbf{\tau}^{Z} \in \mathcal{S}} \delta(\mathbf{\tau}^{Z} - \mathbf{r})$$
(1)

where  $S \subset \mathbb{R}^3$  denotes the set of atom center coordinates relative to the atom of interest (including the atom of interest), and Z denotes the element type. There are two issues with directly adopting eq 1 as a representation of the atomic neighborhood. From an ML perspective, the use of delta functions can cause small perturbations of the atomic positions to result in large changes in model predictions. From a physics perspective, the delta functions are a nonphysical representation of real atoms because they do not account for the physical volume occupied by the atoms. A physics-based representation of a single atom can be obtained using the raised cosine distribution

$$\nu(\mathbf{r}, Z) = \begin{cases} \frac{1}{2R_{\mathrm{a}}^{Z}} \left[ 1 + \cos\left(\frac{|\mathbf{r}|}{R_{\mathrm{a}}^{Z}}\pi\right) \right], & |\mathbf{r}| \leq R_{\mathrm{a}}^{Z} \\ 0, & |\mathbf{r}| > R_{\mathrm{a}}^{Z} \end{cases}$$
(2)

where  $R_a^Z$  is the atomic radius of element Z. We choose the raised cosine distribution to represent atomic volume because it satisfies two important criteria: (1) it smoothly approaches zero at a finite distance, in this case  $R_a^Z$ , and (2) it does not introduce any nonphysical parameters. The atomic neighborhood can then be represented by the convolution of  $\varphi(r,Z)$ and  $\nu(r,Z)$  as

$$\gamma(\mathbf{r}, Z) = \sum_{\mathbf{\tau}^Z \in S} \frac{1}{2R_a^Z} \left[ 1 + \cos \left( \frac{|\mathbf{\tau}^Z - \mathbf{r}|}{R_a^Z} \pi \right) \right] H(R_a^Z - |\mathbf{\tau}^Z - \mathbf{r}|)$$
(3)

where H is the Heaviside step function.

To use eq 3 to describe an atomic neighborhood, one needs to choose the reference axis using the protocols based on nearest neighbors, as described in Supporting Information Section S1. The use of these protocols imparts translational, rotational, and permutational invariance to the description of the atomic neighborhood.

To reflect the lower importance of features far away from the atom of interest, the atomic neighborhood defined above is damped with the normalized raised cosine distribution  $f_d(r) =$  $0.5[1 + \cos(\pi |r|/R_c)]$ , where  $R_c$  is the cutoff distance beyond which atoms are considered non-interacting. We again choose the raised cosine distribution because it smoothly approaches zero at the cutoff distance. This allows for a smooth transition of atoms entering and leaving the boundary of the atomic neighborhood. The damped atomic neighborhood is now expressed as

$$\eta(\mathbf{r}, Z) = \gamma(\mathbf{r}, Z) f_{\mathrm{d}}(\mathbf{r}) \tag{4}$$

A graphical representation of the atomic neighborhood constructed via eqs 1-4 is shown in Figure 1. The VASt

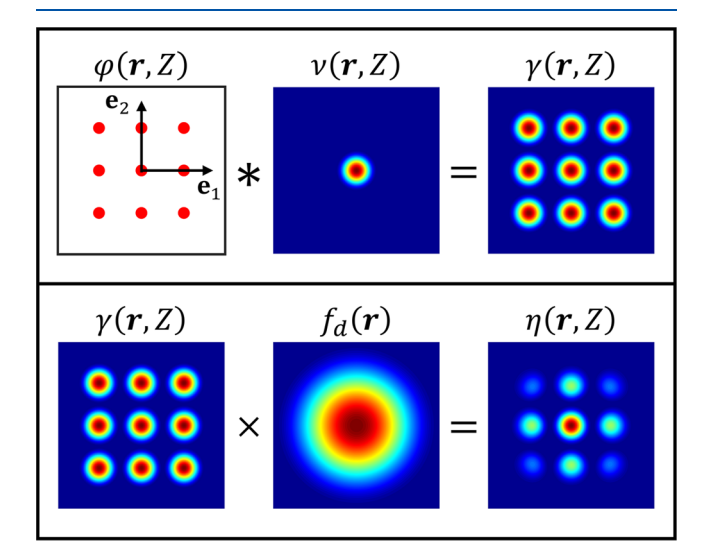


Figure 1. Graphical representation of a two-dimensional atomic neighborhood constructed via eqs 1–4. (top) The atom center coordinates in the neighborhood of the atom of interest (including the atom of interest),  $\varphi(r,Z)$ , are convolved with the raised cosine distribution representation of an atom,  $\nu(r,Z)$ , to produce the undamped atomic neighborhood,  $\gamma(r,Z)$ . (bottom) The undamped atomic neighborhood,  $\gamma(r,Z)$ , is multiplied by the damping function,  $f_{\rm d}(r)$ , to produce the damped atomic neighborhood,  $\eta(r,Z)$ .

representation of the atomic neighborhood is the discretized form of eq 4 and invokes only two nonphysical parameters: the voxel size and the cutoff distance. Further, in the limit as voxel size approaches zero, one recovers the complete continuous representation of the true atomic neighborhood. It is emphasized that eq 4 can resolve infinitesimal perturbations of the atomic structure. In other words, even an infinitesimal

change in any of the atom center positions will change  $\eta(r,Z)$ because of the use of eq 3. It is important to retain this feature in the VASt representation of the atomic neighborhood. This is accomplished by first suitably partitioning each atom to its nearest voxels (based on the atom center coordinates and the coordinates of the nearest voxel centers), producing a digital representation of  $\varphi(r,Z)$ . This digital signal is then convolved (using a fast Fourier transform algorithm) with a suitable digital representation (i.e., uniform sampling) of  $\nu(r,Z)$  to produce a digital representation of  $\gamma(r,Z)$ . Finally, a pointwise multiplication of the digital representations of  $\gamma(r,Z)$  and  $f_d(r)$ produces the desired digital representation of the atomic neighborhood,  $\eta(r,Z)$ . All of the operations described above are computationally very efficient and scale almost linearly with the number of voxels. The images shown in Figure 1 are the digital representations of the various quantities described above.

For the first case study, we develop a single VASt potential capable of predicting highly accurate interatomic forces for both 3C-SiC and 6H-SiC. The framework for developing a VASt potential is shown in Figure 2. First, a set of reference atomic configurations and corresponding ground-truth interatomic forces are generated for training the ML model. Here, reference atomic configurations were generated using AIMD simulations at 300 K, and ground-truth interatomic forces were computed with DFT using the Vienna Ab initio Simulation Package (VASP).<sup>58</sup> A total of 2000 snapshots of the 216-atom  $3 \times 3 \times 3$  3C-SiC supercell and 2225 snapshots of the 192atom  $4 \times 4 \times 1$  6H-SiC supercell were used. We chose to use large supercells because the resulting atomic environments are more disordered than those of small supercells and therefore produce more diverse training and testing data sets. More snapshots of the smaller 6H-SiC supercell are used in order to include an approximately equal number of atomic neighborhoods from each phase. Next, the atomic neighborhoods are mapped to the 3D voxelized domain using the protocols described earlier. Here, R<sub>c</sub> was selected as 8.0 Å, and the 3D atomic neighborhood was discretized into  $97 \times 97 \times 97$  voxels, with a voxel size of  $\sim 0.165$  Å. Finally, the CNN is trained using the reference atomic neighborhoods as the input and their corresponding atomic force vectors as the target. Details of the CNN architecture and training protocols are provided in Supporting Information Section S2 and Figure S1. The accuracy of the VASt potential is evaluated by predicting

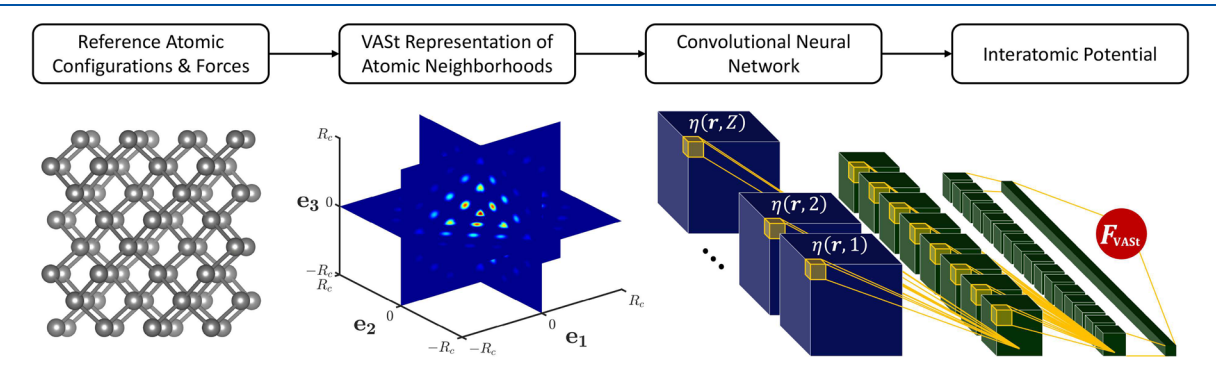


Figure 2. Framework for developing a VASt potential. (left) Reference atomic configurations and corresponding ground-truth interatomic forces are generated for training. (center) The reference atomic neighborhoods are mapped to their VASt representations. A 3D cross-section of a single channel of a VASt atomic neighborhood is shown. (right) The CNN-based interatomic potential is trained. Shown, a VASt atomic neighborhood with Z channels (one for each chemical element) (blue) is input to the CNN (green), which predicts the corresponding interatomic force vector,  $\mathbf{F}_{\text{VASt}}$  (red).

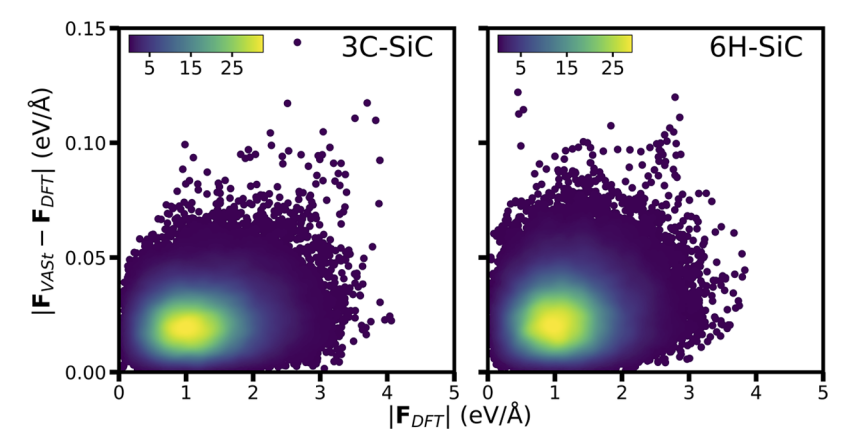


Figure 3. Absolute errors of the VASt force predictions for new (i.e., not used in training) atomic neighborhoods of (left) 3C-SiC and (right) 6H-SiC, relative to their DFT-computed force magnitudes. The color shows the frequency of the samples relative to their absolute errors and DFT-computed force magnitudes. Each phase is normalized individually.

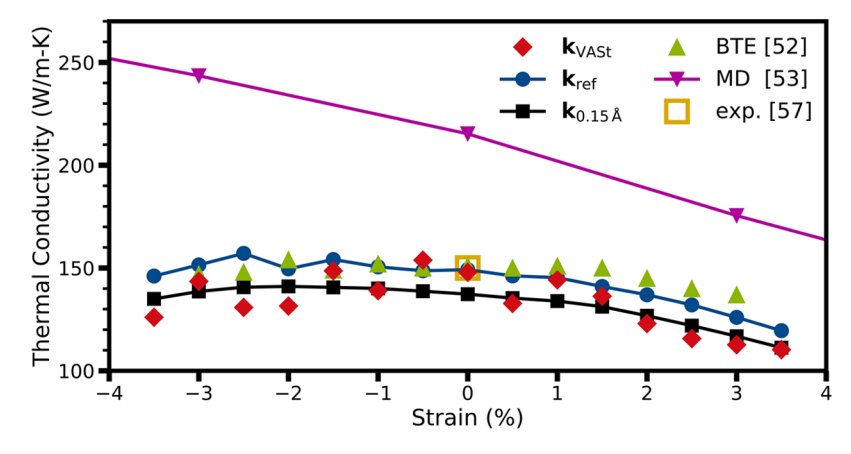


Figure 4. Thermal conductivity of silicon as a function of isotropic strain. The  $k_{VASt}$  is computed with the BTE using IFCs obtained from our VASt potential, while  $k_{ref}$  and  $k_{0.15~\text{Å}}$  are computed with the BTE using IFCs obtained from DFT. The third-order IFC finite displacement distances used for  $k_{VASv}$ ,  $k_{re\theta}$  and  $k_{0.15~\text{Å}}$  are 0.15, 0.01, and 0.15 Å, respectively. The second-order IFC finite displacement distance for  $k_{VASv}$ ,  $k_{re\theta}$  and  $k_{0.15~\text{Å}}$  is 0.01 Å. For comparison, the thermal conductivities computed using DFT with the BTE in ref 52 and using MD in ref 53 are also shown along with the experimental thermal conductivity of unstrained silicon. <sup>57</sup>

interatomic forces on a new set of atomic neighborhoods (i.e., not part of the training data set) generated using separate AIMD simulations at 300 K (separate from those used to generate the training data set). Random initial velocities are used in each AIMD simulation to guarantee that the atomic neighborhoods in the training and testing data sets are sampled from separate and unique trajectories. A total of 500 snapshots of both the 216-atom 3C-SiC and 192-atom 6H-SiC supercells are used. Although here we use the same size supercells for the training and testing data sets, the VASt framework has transferability to atomic systems that are larger than those used for training because of the damping function. In Figure 3, the absolute errors of the VASt force predictions for the new atomic neighborhoods are plotted relative to their DFT computed force magnitudes. The mean absolute errors of the 3C-SiC and 6H-SiC predictions are 0.022 and 0.025 eV/Å, respectively, and the average percent errors (with respect to the DFT-computed force magnitudes) are 2.33% and 2.74%, respectively.

Next, we develop a VASt potential that can rapidly and accurately compute the thermal conductivity of silicon for any isotropic strain in the range from -0.035 to 0.035. The training data set for the VASt potential consists of 6000 configurations of the 216-atom  $3 \times 3 \times 3$  supercell. Details of

the data generation procedure can be found in Supporting Information Section S3. The atomic neighborhoods are mapped to a 3D domain with a larger  $R_c$  of 12 Å in order to capture the long-range phonon interactions. The 3D domain is again discretized into  $97 \times 97 \times 97$  voxels, resulting in a voxel size of  $\sim 0.25$  Å.

The thermal conductivity results are shown in Figure 4. First, a set of reference thermal conductivities,  $k_{\rm ref}$  are computed at 0.005 intervals of isotropic strain ranging from -0.035 to 0.035. The  $k_{\rm ref}$  values are computed using IFCs obtained from interatomic forces calculated with DFT for a finite displacement distance of 0.01 Å. The  $k_{\rm ref}$  are in good agreement with those computed by Parrish et al.<sup>52</sup> using DFT and the BTE; the average and maximum percent differences are  $\sim$ 3.9% and  $\sim$ 8.4%, respectively, for isotropic strain ranging from -0.03 to 0.03 (the full range computed by Parrish et al.<sup>52</sup>).

Next, we compute the thermal conductivities using our VASt potential ( $k_{\text{VASt}}$ ). The VASt potential is used to predict the interatomic forces required for computing the second- and third-order IFCs via the finite displacement method. The typical 0.01 Å finite displacement distance is used for the second-order IFCs, but a larger 0.15 Å finite displacement distance is used for the third-order IFCs. We found that this

significantly reduced the sensitivity of the third-order IFCs to noise without introducing significant error. For isotropic strain ranging from -0.035 to 0.035, the average and maximum percent errors between the  $k_{\rm ref}$  and the thermal conductivities computed using IFCs obtained from DFT with a 0.15 Å third-order IFC finite displacement distance  $(k_{0.15}$  Å) are  $\sim$ 7.6% and  $\sim$ 10.5%, respectively.

The  $k_{\text{VASt}}$  are observed to be in excellent agreement with the  $k_{0.15 \text{ Å}}$ . For isotropic strain ranging from -0.035 to 0.035, the average and maximum percent errors are ~5.0% and ~10.9%, respectively. Furthermore, the thermal conductivities predicted by our VASt potential accurately capture the trend of relatively constant thermal conductivity from compression to equilibrium and decreasing thermal conductivity from equilibrium to tension (see Figure 4). The predictions from the VASt potential are also a substantial improvement over those from MD with the Tersoff empirical potential.<sup>53</sup> Relative to the  $k_{ref}$ the thermal conductivities estimated from MD for isotropic strain ranging from -0.03 to 0.03 have an average and maximum error of ~48.1% and ~60.7%, respectively, and falsely show thermal conductivity monotonically decreasing from compression to tension. Furthermore, the percent error between the VASt-predicted thermal conductivity for unstrained silicon (147.9 W/m K) and the experimental thermal conductivity  $(\sim 150 \text{ W/m K})^{57}$  is only  $\sim 1.4\%$ , whereas the percent error between the MD predicted thermal conductivity (~215 W/m K)<sup>53</sup> and experimental thermal conductivity is ~43.5%. Given the highly sensitive nature of the third-order IFCs, the success with which our VASt potential reproduces thermal conductivity over a continuous range of isotropic strain is truly remarkable. In particular, we note that the 0.01 Å second-order and 0.15 Å third-order finite displacement distances are both smaller than the ~0.25 Å voxel size of the 3D voxelized domain. This proves that VASt potentials are able to capture perturbations of atomic structure much smaller than the voxel size. To further emphasize this point, we also use this VASt potential to reproduce the unstrained silicon phonon dispersion curve (which depends only on the second-order IFCs) and observe that it is in excellent agreement with the phonon dispersion curve computed using IFCs obtained from DFT (see Figure S2).

In conclusion, we have introduced VASt potentials, a deep learning framework for developing ML-based interatomic potentials. By directly capturing the true atomic structure on a voxelized 3D domain, VASt potentials are able to leverage the comprehensive, automated, scalable, and highly efficient feature engineering capabilities of CNNs to implicitly learn the complex spatial relationships and multibody interactions that govern the physics of atomic systems. We first demonstrate that VASt potentials accurately capture a diverse set of atomic configurations by producing a single VASt potential capable of predicting highly accurate interatomic forces on two phases of a multicomponent system. We then demonstrate that, in addition to capturing a diverse set of atomic configurations, VASt potentials are simultaneously sensitive to small perturbations of atomic structure (much less than the voxel size) by developing a VASt potential capable of accurately reproducing the thermal conductivity of silicon subjected to isotropic strain ranging from -0.035 to 0.035. We show that the thermal conductivities computed within this range are substantially more accurate than those computed using MD with the Tersoff potential.

#### COMPUTATIONAL METHODS

Density functional theory calculations are performed using VASP. A plane-wave basis set and the projector augmented-wave method are used with the Perdew–Burke–Ernzerhof generalized gradient approximation exchange-correlation functional. For all calculations, the convergence criteria for the energy and force is  $10^{-8}$  eV and  $10^{-6}$  eV/Å, respectively.

The plane-wave basis cutoff energy for all SiC calculations is 520 eV. The 3C-SiC and 6H-SiC unit cell structures are optimized using 27  $\times$  27  $\times$  27 and 27  $\times$  27  $\times$  3  $\Gamma$ -centered grids of k-points, respectively. Atomic configurations of the 3  $\times$  3  $\times$  3 3C-SiC and 4  $\times$  4  $\times$  1 6H-SiC supercells are obtained using AIMD. The AIMD simulations are performed using the NVT thermostat at 300 K with a time step of 1 fs. The snapshots for the training and validation data sets are selected every 4 fs (i.e., four time steps) to allow for higher variance in the atomic configurations. The atomic forces are computed using a 3  $\times$  3  $\times$  3  $\Gamma$ -centered grid of k-points for both phases.

The plane-wave basis cutoff energy for all silicon calculations is 320 eV. The unstrained cubic diamond silicon unit cell is optimized using a  $27 \times 27 \times 27$   $\Gamma$ -centered grid of k-points. The unstrained lattice constant obtained using DFT is 5.47 Å. Isotropic strain is applied by changing the lattice constant according to  $a = a_0(1+\varepsilon)$ , where  $a_0$  is the unstrained lattice constant. The DFT-computed IFCs and the training data are both calculated using the  $3 \times 3 \times 3$  silicon supercell with a  $3 \times 3 \times 3$   $\Gamma$ -centered grid of k-points. The thermal conductivity is computed using Fermi's golden rule<sup>63</sup> with the iterative solution to the BTE. Fermi's golden rule<sup>63</sup> with the iterative solution to the BTE. Fermi's golden rule for the 3 × 3 × 3 silicon supercell using the finite displacement method. Second-order anharmonic IFCs are computed for the 3 × 3 × 3 silicon supercell using the finite displacement method. Second-order IFCs are computed for the third-order IFCs.

## ASSOCIATED CONTENT

# **5** Supporting Information

The Supporting Information is available free of charge at https://pubs.acs.org/doi/10.1021/acs.jpclett.0c02271.

Details on constructing the reference axis of an atomic neighborhood, details of the CNN architecture and training protocols, details of the silicon data generation procedure, figure of CNN architecture, figure of silicon phonon dispersion curve (PDF)

#### AUTHOR INFORMATION

#### **Corresponding Authors**

Matthew C. Barry — G.W. Woodruff School of Mechanical Engineering, Georgia Institute of Technology, Atlanta, Georgia 30332, United States; orcid.org/0000-0003-1932-1456; Email: mbarry31@gatech.edu

Satish Kumar — G.W. Woodruff School of Mechanical Engineering, Georgia Institute of Technology, Atlanta, Georgia 30332, United States; Email: satish.kumar@me.gatech.edu

# **Authors**

Kristopher E. Wise – Advanced Materials and Processing Branch, NASA Langley Research Center, Hampton, Virginia 23681, United States

Surya R. Kalidindi — G.W. Woodruff School of Mechanical Engineering, Georgia Institute of Technology, Atlanta, Georgia 30332, United States

Complete contact information is available at:

https://pubs.acs.org/10.1021/acs.jpclett.0c02271

#### Notes

The authors declare no competing financial interest.

#### ACKNOWLEDGMENTS

This work was supported by a NASA Space Technology Research Fellowship and by the National Science Foundation under Grant No. 1258425. This work used computer resources supported by the National Science Foundation under Grant No. 1828187.

### REFERENCES

- (1) Kohn, W.; Sham, L. J. Self-Consistent Equations Including Exchange and Correlation Effects. *Phys. Rev.* **1965**, *140*, A1133–A1138
- (2) Payne, M. C.; Teter, M. P.; Allan, D. C.; Arias, T. A.; Joannopoulos, J. D. Iterative Minimization Techniques for Ab Initio Total-Energy Calculations: Molecular Dynamics and Conjugate Gradients. *Rev. Mod. Phys.* **1992**, *64*, 1045–1097.
- (3) Ercolessi, F.; Adams, J. B. Interatomic Potentials from First-Principles Calculations: The Force-Matching Method. *Europhys. Lett.* **1994**, *26*, 583–588.
- (4) Bazant, M. Z.; Kaxiras, E.; Justo, J. F. Environment-Dependent Interatomic Potential for Bulk Silicon. *Phys. Rev. B: Condens. Matter Mater. Phys.* 1997, 56, 8542–8552.
- (5) Mishin, Y.; Farkas, D.; Mehl, M. J.; Papaconstantopoulos, D. A. Interatomic Potentials for Monoatomic Metals from Experimental Data and Ab Initio Calculations. *Phys. Rev. B: Condens. Matter Mater. Phys.* 1999, 59, 3393–3407.
- (6) van Duin, A. C. T.; Dasgupta, S.; Lorant, F.; Goddard, W. A. ReaxFF: A Reactive Force Field for Hydrocarbons. J. Phys. Chem. A 2001, 105, 9396-9409.
- (7) Vanommeslaeghe, K.; Hatcher, E.; Acharya, C.; Kundu, S.; Zhong, S.; Shim, J.; Darian, E.; Guvench, O.; Lopes, P.; Vorobyov, I.; et al. CHARMM General Force Field: A Force Field for Drug-Like Molecules Compatible with the CHARMM All-Atom Additive Biological Force Fields. *J. Comput. Chem.* **2009**, *31*, *671*–690.
- (8) Wang, J.; Wolf, R. M.; Caldwell, J. W.; Kollman, P. A.; Case, D. A. Development and Testing of a General Amber Force Field. *J. Comput. Chem.* **2004**, *25*, 1157–1174.
- (9) Daw, M. S.; Baskes, M. I. Embedded-Atom Method: Derivation and Application to Impurities, Surfaces, and Other Defects in Metals. *Phys. Rev. B: Condens. Matter Mater. Phys.* **1984**, *29*, 6443–6453.
- (10) Brenner, D. W.; Shenderova, O. A.; Harrison, J. A.; Stuart, S. J.; Ni, B.; Sinnott, S. B. A Second-Generation Reactive Empirical Bond Order (REBO) Potential Energy Expression for Hydrocarbons. *J. Phys.: Condens. Matter* **2002**, *14*, 783–802.
- (11) Stillinger, F. H.; Weber, T. A. Computer Simulation of Local Order in Condensed Phases of Silicon. *Phys. Rev. B: Condens. Matter Mater. Phys.* 1985, 31, 5262–5271.
- (12) Tersoff, J. Modeling Solid-State Chemistry: Interatomic Potentials for Multicomponent Systems. *Phys. Rev. B: Condens. Matter Mater. Phys.* **1989**, *39*, 5566–5568.
- (13) Saal, J. E.; Kirklin, S.; Aykol, M.; Meredig, B.; Wolverton, C. Materials Design and Discovery with High-Throughput Density Functional Theory: The Open Quantum Materials Database (OQMD). *JOM* **2013**, *65*, 1501–1509.
- (14) Lee, J.; Seko, A.; Shitara, K.; Nakayama, K.; Tanaka, I. Prediction Model of Band Gap for Inorganic Compounds by Combination of Density Functional Theory Calculations and Machine Learning Techniques. *Phys. Rev. B: Condens. Matter Mater. Phys.* **2016**, 93, 115104.
- (15) Ward, L.; Agrawal, A.; Choudhary, A.; Wolverton, C. A General-Purpose Machine Learning Framework for Predicting Properties of Inorganic Materials. *npj Comput. Mater.* **2016**, *2*, 16028.

- (16) Pilania, G.; Gubernatis, J. E.; Lookman, T. Multi-Fidelity Machine Learning Models for Accurate Bandgap Predictions of Solids. *Comput. Mater. Sci.* **2017**, *129*, 156–163.
- (17) Kim, C.; Chandrasekaran, A.; Huan, T. D.; Das, D.; Ramprasad, R. Polymer Genome: A Data-Powered Polymer Informatics Platform for Property Predictions. *J. Phys. Chem. C* **2018**, *122*, 17575–17585.
- (18) Meredig, B.; Agrawal, A.; Kirklin, S.; Saal, J. E.; Doak, J. W.; Thompson, A.; Zhang, K.; Choudhary, A.; Wolverton, C. Combinatorial Screening for New Materials in Unconstrained Composition Space with Machine Learning. *Phys. Rev. B: Condens. Matter Mater. Phys.* **2014**, 89, 094104.
- (19) Gubaev, K.; Podryabinkin, E. V.; Hart, G. L. W.; Shapeev, A. V. Accelerating High-Throughput Searches for New Alloys with Active Learning of Interatomic Potentials. *Comput. Mater. Sci.* **2019**, *156*, 148–156.
- (20) Gilmer, J.; Schoenholz, S. S.; Riley, P. F.; Vinyals, O.; Dahl, G. E. Neural Message Passing for Quantum Chemistry. *arXiv* (*Machine Learning*) 2017, 1704.01212. https://arxiv.org/abs/1704.01212 (accessed on Oct 1, 2020)
- (21) Duvenaud, D. K.; Maclaurin, D.; Iparraguirre, J.; Bombarell, R.; Hirzel, T.; Aspuru-Guzik, A.; Adams, R. P. Convolutional Networks on Graphs for Learning Molecular Fingerprints. *Advances in Neural Information Processing Systems* **2015**, 2224–2232.
- (22) Behler, J.; Parrinello, M. Generalized Neural-Network Representation of High-Dimensional Potential-Energy Surfaces. *Phys. Rev. Lett.* **2007**, 98, 146401.
- (23) Batra, R.; Tran, H. D.; Kim, C.; Chapman, J.; Chen, L.; Chandrasekaran, A.; Ramprasad, R. General Atomic Neighborhood Fingerprint for Machine Learning-Based Methods. *J. Phys. Chem. C* **2019**, *123*, 15859–15866.
- (24) Li, Z.; Kermode, J. R.; De Vita, A. Molecular Dynamics with On-the-Fly Machine Learning of Quantum-Mechanical Forces. *Phys. Rev. Lett.* **2015**, *114*, 096405.
- (25) Bartók, A. P.; Payne, M. C.; Kondor, R.; Csányi, G. Gaussian Approximation Potentials: The Accuracy of Quantum Mechanics, without the Electrons. *Phys. Rev. Lett.* **2010**, *104*, 136403.
- (26) Thompson, A. P.; Swiler, L. P.; Trott, C. R.; Foiles, S. M.; Tucker, G. J. Spectral Neighbor Analysis Method for Automated Generation of Quantum-Accurate Interatomic Potentials. *J. Comput. Phys.* **2015**, 285, 316–330.
- (27) Shapeev, A. V. Moment Tensor Potentials: A Class of Systematically Improvable Interatomic Potentials. *Multiscale Model. Simul.* **2016**, *14*, 1153–1173.
- (28) Bartók, A. P.; Kondor, R.; Csányi, G. On Representing Chemical Environments. *Phys. Rev. B: Condens. Matter Mater. Phys.* **2013**, 87, 184115.
- (29) Zhang, L.; Han, J.; Wang, H.; Car, R.; E, W. Deep Potential Molecular Dynamics: A Scalable Model with the Accuracy of Quantum Mechanics. *Phys. Rev. Lett.* **2018**, *120*, 143001.
- (30) Wang, Z.; Han, Y.; Li, J.; He, X. Combining the Fragmentation Approach and Neural Network Potential Energy Surfaces of Fragments for Accurate Calculation of Protein Energy. *J. Phys. Chem. B* **2020**, *124*, 3027–3035.
- (31) Schütt, K. T.; Arbabzadah, F.; Chmiela, S.; Müller, K. R.; Tkatchenko, A. Quantum-Chemical Insights from Deep Tensor Neural Networks. *Nat. Commun.* **2017**, *8*, 13890.
- (32) Schütt, K. T.; Sauceda, H. E.; Kindermans, P.-J.; Tkatchenko, A.; Müller, K.-R. SchNet A Deep Learning Architecture for Molecules and Materials. *J. Chem. Phys.* **2018**, *148*, 241722.
- (33) Smith, J. S.; Isayev, O.; Roitberg, A. E. ANI-1: An Extensible Neural Network Potential with DFT Accuracy at Force Field Computational Cost. *Chem. Sci.* **2017**, *8*, 3192–3203.
- (34) Lubbers, N.; Smith, J. S.; Barros, K. Hierarchical Modeling of Molecular Energies Using a Deep Neural Network. *J. Chem. Phys.* **2018**, *148*, 241715.
- (35) Xie, T.; France-Lanord, A.; Wang, Y.; Shao-Horn, Y.; Grossman, J. C. Graph Dynamical Networks for Unsupervised Learning of Atomic Scale Dynamics in Materials. *Nat. Commun.* **2019**, *10*, 2667.

- (36) Huan, T. D.; Batra, R.; Chapman, J.; Krishnan, S.; Chen, L.; Ramprasad, R. A Universal Strategy for the Creation of Machine Learning-Based Atomistic Force Fields. *npj Comput. Mater.* **2017**, 3, 37.
- (37) Behler, J. Atom-Centered Symmetry Functions for Constructing High-Dimensional Neural Network Potentials. *J. Chem. Phys.* **2011**, *134*, 074106.
- (38) Botu, V.; Ramprasad, R. Learning Scheme to Predict Atomic Forces and Accelerate Materials Simulations. *Phys. Rev. B: Condens. Matter Mater. Phys.* **2015**, 92, 094306.
- (39) Korotaev, P.; Novoselov, I.; Yanilkin, A.; Shapeev, A. Accessing Thermal Conductivity of Complex Compounds by Machine Learning Interatomic Potentials. *Phys. Rev. B: Condens. Matter Mater. Phys.* **2019**, *100*, 144308.
- (40) Babaei, H.; Guo, R.; Hashemi, A.; Lee, S. Machine-Learning-Based Interatomic Potential for Phonon Transport in Perfect Crystalline Si and Crystalline Si with Vacancies. *Phys. Rev. Mater.* **2019**, *3*, 074603.
- (41) Rupp, M.; Tkatchenko, A.; Müller, K.-R.; von Lilienfeld, O. A. Fast and Accurate Modeling of Molecular Atomization Energies with Machine Learning. *Phys. Rev. Lett.* **2012**, *108*, 058301.
- (42) Chmiela, S.; Tkatchenko, A.; Sauceda, H. E.; Poltavsky, I.; Schütt, K. T.; Müller, K.-R. Machine Learning of Accurate Energy-Conserving Molecular Force Fields. *Sci. Adv.* **2017**, *3*, No. e1603015.
- (43) Bartók, A. P.; Kermode, J.; Bernstein, N.; Csányi, G. Machine Learning a General-Purpose Interatomic Potential for Silicon. *Phys. Rev. X* **2018**, *8*, 041048.
- (44) Dragoni, D.; Daff, T. D.; Csányi, G.; Marzari, N. Achieving DFT Accuracy with a Machine-Learning Interatomic Potential: Thermomechanics and Defects in Bcc Ferromagnetic Iron. *Phys. Rev. Mater.* **2018**, *2*, 013808.
- (45) Kolb, B.; Lentz, L. C.; Kolpak, A. M. Discovering Charge Density Functionals and Structure-Property Relationships with PROPhet: A General Framework for Coupling Machine Learning and First-Principles Methods. *Sci. Rep.* **2017**, *7*, 1192.
- (46) LeCun, Y.; Bottou, L.; Bengio, Y.; Haffner, P. Gradient-Based Learning Applied to Document Recognition. *Proc. IEEE* **1998**, *86*, 2278–2324.
- (47) Krizhevsky, A.; Sutskever, I.; Hinton, G. E. ImageNet Classification with Deep Convolutional Neural Networks. *Commun. ACM* **2017**, *60*, 1097–1105.
- (48) Szegedy, C.; Liu, W.; Jia, Y.; Sermanet, P.; Reed, S.; Anguelov, D.; Erhan, D.; Vanhoucke, V.; Rabinovich, A. Going Deeper with Convolutions. *Proceedings of the IEEE Conference on Computer Vision and Pattern Recognition*, Boston, MA, June 7–12, 2015; IEEE, 2015; pp 1–9. DOI: 10.1109/CVPR.2015.7298594
- (49) Simonyan, K.; Zisserman, A. Very Deep Convolutional Networks for Large-Scale Image Recognition. arXiv (Computer Vision and Pattern Recognition), 2014, 1409.1556.https://arxiv.org/abs/1409.1556 (accessed on Oct 1, 2020)
- (50) He, K.; Zhang, X.; Ren, S.; Sun, J. Deep Residual Learning for Image Recognition. In *Proceedings of the IEEE Conference on Computer Vision and Pattern Recognition*, Las Vegas, NV, 2016; IEEE, 2016; pp 770–778. DOI: 10.1109/CVPR.2016.90
- (51) Car, R.; Parrinello, M. Unified Approach for Molecular Dynamics and Density-Functional Theory. *Phys. Rev. Lett.* **1985**, *55*, 2471–2474.
- (52) Parrish, K. D.; Jain, A.; Larkin, J. M.; Saidi, W. A.; McGaughey, A. J. H. Origins of Thermal Conductivity Changes in Strained Crystals. *Phys. Rev. B: Condens. Matter Mater. Phys.* **2014**, *90*, 235201.
- (53) Li, X.; Maute, K.; Dunn, M. L.; Yang, R. Strain Effects on the Thermal Conductivity of Nanostructures. *Phys. Rev. B: Condens. Matter Mater. Phys.* **2010**, *81*, 245318.
- (54) Yan, Z.; Kumar, S. Phonon Mode Contributions to Thermal Conductivity of Pristine and Defective  $\beta$ -Ga<sub>2</sub>O<sub>3</sub>. *Phys. Chem. Chem. Phys.* **2018**, 20, 29236–29242.
- (55) Barry, M. C.; Yan, Z.; Yoon, M.; Kalidindi, S. R.; Kumar, S. Phonon Transport Properties of Two-Dimensional Electride Ca<sub>2</sub>N—A First-Principles Study. *Appl. Phys. Lett.* **2018**, *113*, 131902.

- (56) Broido, D. A.; Ward, A.; Mingo, N. Lattice Thermal Conductivity of Silicon from Empirical Interatomic Potentials. *Phys. Rev. B: Condens. Matter Mater. Phys.* **2005**, 72, 014308.
- (57) Glassbrenner, C. J.; Slack, G. A. Thermal Conductivity of Silicon and Germanium from 3 K to the Melting Point. *Phys. Rev.* **1964**, 134, A1058–A1069.
- (58) Kresse, G.; Furthmüller, J. Efficient Iterative Schemes for Ab Initio Total-Energy Calculations Using a Plane-Wave Basis Set. *Phys. Rev. B: Condens. Matter Mater. Phys.* **1996**, *54*, 11169–11186.
- (59) Togo, A.; Tanaka, I. First Principles Phonon Calculations in Materials Science. *Scr. Mater.* **2015**, *108*, 1–5.
- (60) Blöchl, P. E. Projector Augmented-Wave Method. Phys. Rev. B: Condens. Matter Mater. Phys. 1994, 50, 17953–17979.
- (61) Kresse, G.; Joubert, D. From Ultrasoft Pseudopotentials to the Projector Augmented-Wave Method. *Phys. Rev. B: Condens. Matter Mater. Phys.* **1999**, *59*, 1758–1775.
- (62) Perdew, J. P.; Burke, K.; Ernzerhof, M. Generalized Gradient Approximation Made Simple. *Phys. Rev. Lett.* **1996**, *77*, 3865–3868.
- (63) Maradudin, A. A.; Fein, A. E. Scattering of Neutrons by an Anharmonic Crystal. *Phys. Rev.* **1962**, *128*, 2589–2608.
- (64) Li, W.; Carrete, J.; A Katcho, N.; Mingo, N. ShengBTE: A Solver of the Boltzmann Transport Equation for Phonons. *Comput. Phys. Commun.* **2014**, *185*, 1747–1758.
- (65) Li, W.; Mingo, N.; Lindsay, L.; Broido, D. A.; Stewart, D. A.; Katcho, N. A. Thermal Conductivity of Diamond Nanowires from First Principles. *Phys. Rev. B: Condens. Matter Mater. Phys.* **2012**, 85, 195436.
- (66) Li, W.; Lindsay, L.; Broido, D. A.; Stewart, D. A.; Mingo, N. Thermal Conductivity of Bulk and Nanowire Mg<sub>2</sub>Si<sub>x</sub>Sn<sub>1-x</sub> Alloys from First Principles. *Phys. Rev. B: Condens. Matter Mater. Phys.* **2012**, *86*, 174307.